Numerical computation of the sensitivity kernel for time-lapse monitoring with multiply scattered waves

Chinaemerem Kanu and Roel Snieder
Center for Wave Phenomena, Colorado School of Mines, Golden CO 80401

ABSTRACT
In time-lapse monitoring of weak localized changes within a medium using coda waves, we can either use the resulting decorrelation and/or the phase shift of the coda waves. The formulation for both the decorrelation and the phase-shift of the coda waves resulting from the weak time-lapse changes contains a common sensitivity kernel that is needed to image the weak localized changes. We provide a novel approach to compute the sensitivity kernel which uses numerical modeling (finite difference) of the wavefields from the source and the receiver with an a prior scattering model. These wavefields give the intensities needed to compute the sensitivity kernels. This approach is different from common methods of computing the sensitivity kernel that use analytical approximations of the scattered intensity. The numerical solution of the sensitivity kernel allows us to use arbitrary earth model that may include a free surface without simplifying the property of the scattering model. We demonstrate the behavior of the numerical solution of the sensitivity kernel with end members of heterogeneous scattering models.

1 INTRODUCTION

Multiple scattering of seismic waves along their travel paths potentially provides information about the subsurface that can be used to increase the resolution of an imaged subsurface (with multiple reflected waves) (*Belkebir et al.*, 2006), increase illumination especially within a poorly illuminated subsurface (*Gaburro et al.*, 2007; *Fleury*, 2013) and monitor weak time-lapse changes within the earth's subsurface (*Poupinet et al.*, 1984; *Snieder et al.*, 2002; *Schaff and Beroza*, 2004). Using scattered waves, especially for monitoring temporal weak changes within the subsurface, we can increase the illumination and resolution of time-lapse changes within a subsurface (*Malcolm et al.*, 2009; *Berkhout et al.*, 2012). Multiply scattered waves are used for monitoring weak changes such as velocity changes as weak as 0.1% (*Snieder et al.*, 2002) and monitoring defects within mechanical structures (*Masera et al.*, 2011). However, the complexity in the travel paths of the multiply scattered waves, which depends on the scattering properties of the medium of interest, makes it challenging to accurately describe the origin, travel paths, and distribution of the scattered waves within the medium. In a strongly scattering medium, the multiply scattered waves for late lapse time can be described as a diffusive process (*Wesley*, 1965; *Shapiro and Kneib*, 1993; *Page et al.*, 1995). The diffusion model has been used successfully in imaging algorithms that use multiply scattered waves in medical imaging (*Yodh and Chance*, 1995) or in imaging of missing scatterers (*Rossetto et al.*, 2011). But, the validity of using the diffusion intensity model in explaining the multiple scattering of waves depends on the strength of the scattering process. Even in a strongly scattering medium, the diffusion intensity model is only accurate at large lapse times, i.e. for $t >> r/c$, where t is the travel-time, r is the source-receiver distance and c is the average velocity of the medium. Alternatively, the scattered intensity can be modeled using the radiative transfer intensity model, which more accurately predicts the scattered intensity for all scattering regimes (*Paasschens*, 1997; *Turner and Weaver*, 1994). The diffusion and radiative transfer intensity models are analytical models developed under the assumption of a stochastic wave equation. These analytical intensity models, as well as most other intensity models for the scattered waves, are based on homogeneous or simple scattering media. The scattered intensity can easily become complicated if the statistical properties of the scattering medium are heterogeneous. We show that for more realistic media, a more accurate scattered intensity can be modeled numerically using, for example, finite-difference modeling rather than using the analytical intensity models.

Time-lapse changes within the earth's subsurface (both natural and induced) are usually either gradual, weak, or localized both in space and time. Detecting these changes in many cases requires data that are highly sensitive to the changes. *Vlastos et al.* (2006)

show that the sensitivity of multiply scattered waves to the weak changes is significantly higher than the sensitivity of the ballistic or direct part of the seismic waves to the weak changes. This increase in the sensitivity is due to the repeated sampling of the weak velocity changes by the scattered waves (*Rossetto*, 2013). The high sensitivity of the multiply scattered waves has led to successful detection of time-lapse velocity changes within the earth's subsurface. *Poupinet et al.* (1984) use coda waves generated by repeating earthquakes to observe an average S wave velocity change of 0.2% after the 1979 M_w 5.9 Coyote Lake earthquake on the Calaveras Fault, California. Using correlation functions generated from seismic noise, *Wegler and Sens-Schnfelder* (2007) detect a sudden decrease in the seismic velocity of the region surrounding the 2004 M_w 6.6 Mid-Niigata earthquake rupture. Using controlled-source monitoring *Nishimura et al.* (2000) detected a velocity decrease of 0.3-1.0 % due to the 1998 M_w 6.1 Mount Iwate earthquake. However, *Pacheco and Snieder* (2005) show that the spatial sensitivity of the multiply scattered waves to the time lapse changes is not uniformly distributed but is dependent on the source and receiver locations.

Most time-lapse monitoring of weak changes within the earth's subsurface using multiply scattered waves has been limited to identifying weak changes rather than localizing these changes. Except in very densely distributed source and receiver set-ups, the velocity changes detected by coda wave interferometry are spatially averaged velocity changes. Recently, successful efforts have been made not only in identifying the weak changes using multiply scattered waves, but also in localizing the changes in a statistically homogeneous scattering medium (*Rossetto et al.*, 2011). However, to localize changes within the earth's subsurface - a scattering medium which is most likely to be inhomogenous - we will need to appropriately handle the inhomogeneities of the earth's subsurface. Because of the prominence of surface waves, we also need to account for the presence of a free surface.

In this study, we explore the capability of computing the sensitivity kernel that we need for time-lapse monitoring and localizing the weak changes within a medium. In the next section, we describe the theoretical connection of the sensitivity kernel to the estimated time lapse time-shifts or the decorrelations in the time lapse scattered waves resulting from the weak changes. In section 3, we develop a novel approach for computing the kernel numerically for any scattering model and explore the behavior of the kernel using various end-member scattering models. In section 4, we discuss the practicality of the kernel computation.

2 SENSITIVITY KERNEL

Pacheco and Snieder (2005) use the intensity of multiply scattered waves to develop a sensitivity kernel $K(\mathbf{s}, \mathbf{x_o}, \mathbf{r}, t)$ which relates the mean travel time changes $\langle\tau\rangle$ to the localized relative velocity change within the subsurface $\delta v/v(\mathbf{x_o})$:

$$\langle\tau(t)\rangle = -\int_V K(\mathbf{s}, \mathbf{x_o}, \mathbf{r}, t)\frac{\delta v}{v}(\mathbf{x_o})\,\mathrm{d}V(\mathbf{x_o}), \quad (1)$$

where t is the travel-time of the scattered wave, V is the scattering volume, and $\mathbf{s}$ and $\mathbf{r}$ are the source and the receiver locations, respectively. The sensitivity kernel $K(\mathbf{s}, \mathbf{x_o}, \mathbf{r}, t)$ depends on the source and receiver locations, the scattering property of the medium, and the travel-time of the scattered wave.

Rossetto et al. (2011) consider a different problem where the local scattering strength changes. This change is accounted for by a change in scattering cross-section $\delta\sigma(\mathbf{x_o})$. Using the correlation function $C(\mathbf{s}, \mathbf{r}, t)$ of the multiply scattered waves in a medium with this time-lapse change, they relate the decorrelation $1 - C(\mathbf{s}, \mathbf{r}, t)$ of the time lapse scattered waves to the time lapse change in the total scattering cross-section of the medium:

$$1 - C(\mathbf{s}, \mathbf{r}, t) = \int_V \frac{v(\mathbf{x_o})\delta\sigma(\mathbf{x_o})}{2} K(\mathbf{s}, \mathbf{x_o}, \mathbf{r}, t)\,dV(\mathbf{x_o}). \quad (2)$$

Using either the time-shifts or the decorrelation values from the time-lapse multiply scattered waves for resolving localized weak changes, the sensitivity kernel $K(\mathbf{s}, \mathbf{x_o}, \mathbf{r}, t)$ forms the building block for the Frèchet derivatives needed to resolve the weak changes. The sensitivity kernel $K(\mathbf{s}, \mathbf{x_o}, \mathbf{r}, t)$ is given by

$$K(\mathbf{s}, \mathbf{x_o}, \mathbf{r}, t) = \frac{\int_0^t P(\mathbf{s}, \mathbf{x_o}, t')P(\mathbf{x_o}, \mathbf{r}, t - t')\,\mathrm{d}t'}{P(\mathbf{s}, \mathbf{r}, t)}, \quad (3)$$

where P is the normalized intensity of the multiply scattered waves (*Pacheco and Snieder*, 2005).

The normalized intensity in a homogeneous scattering medium in the diffusion approximation is given by (*Paasschens*, 1997):

$$P(\mathbf{s}, \mathbf{r}, t) = \frac{1}{(4\pi Dt)^{d/2}} \exp\left(-\frac{R_{sr}^2}{4Dt}\right), \quad (4)$$

where d is the dimension of the scattering medium, $R_{sr} = |\mathbf{r} - \mathbf{s}|$ is the source-receiver distance and D is the diffusion coefficient. The normalized intensity can also be described by the radiative transfer model. The 2D radiative transfer intensity (*Paasschens*, 1997) is

$$\begin{aligned} P(\mathbf{s}, \mathbf{r}, t) = {} & \frac{exp(-vt/l)}{2\pi R_{sr}}\delta(vt - R_{sr}) + \\ & \frac{1}{2\pi lvt}\left(1 - R_{sr}^2/v^2t^2\right)^{-1/2} \times \\ & exp\left(\sqrt{v^2t^2 - R_{sr}^2}/l - vt\right)\Theta(vt - R_{sr}), \end{aligned} \quad (5)$$

where l is the scattering mean free path; δ and Θ are the Dirac delta and the Heaviside step functions, respectively. Complex heterogeneous models require a more complex mathematical intensity model to describe

the intensity of the scattered waves (*Margerin and Sato*, 2011). These complex heterogeneous media include heterogeneously layered media (*Margerin et al.*, 1998; *Haney et al.*, 2005) and media with nondiffusive regions (*Ripoll et al.*, 2001). In addition, one may also need to account for the presence of a free surface.

3 NUMERICAL COMPUTATION

For most scattering media, especially for complex heterogeneous scattering media, one might need to compute the sensitivity kernel $K(\mathbf{s}, \mathbf{x_o}, \mathbf{r}, t)$ numerically. For these scattering media, one might not have an exact analytical formulation for either the intensity of the scattered waves or the corresponding sensitivity kernel for imaging the weak changes. Using equation 3 and a model of the scattering medium, we can numerically compute the sensitivity kernel by simulating the scattered wavefield with the scattering model, then compute the intensity field from the simulated wavefield. However, the numerical computation of the sensitivity kernel depends on how well one knows the statistical properties of the scattering medium. The characteristics of the heterogeneous medium, such as the scattering mean free path length and the average velocity, can be estimated from the analysis of the coda waves in the recorded data or using additional information such as velocity values from well log measurements when available or a velocity model obtained from other geophysical methods.

In the following section, we compute the sensitivity kernel using equation 3. We generate the source and receiver wavefields by numerical computation of waves excited at the source and receiver locations, respectively. Here, we use acoustic modeling. We also use absorbing boundary conditions at the boundaries of our models. We do not account of effects due free-surface boundary conditions except in the model with variable topography (section 3.3). The respective normalized intensities are the square of the envelope of the generated wavefields normalized by the spatial integral of the intensity $\int_V P(\mathbf{x_o}, t)\, dV(\mathbf{x_o})$ (*Sato et al.*, 2012). The normalization of the scattered intensity removes imprint of the the source time function from the acoustic intensity field. To compute the sensitivity kernel $K(\mathbf{s}, \mathbf{x_o}, \mathbf{r}, t)$, we convolve the source and the receiver intensity fields and normalize with the denominator in equation 3. We simulate the wavefields with finite difference modeling using a realization of a von-Karman random velocity model (*Sato et al.*, 2012). The 2D von-Karman power spectral density function (PSDF) $\tilde{P}_{2D}$ is given by

$$\tilde{P}_{2D}(k_x, k_z) = \frac{4\pi\Gamma(\kappa+1)\epsilon^2\sqrt{a_x^2 + a_z^2}}{\Gamma(\kappa)(1 + [k_x^2 a_x^2 + k_z^2 a_z^2])^{\kappa+1}}, \quad (6)$$

where κ is the von-Karman exponent, ϵ is the fluctuation strength of the scattering model, a_x and a_z are the correlation lengths along the x- and z- directions, respectively, and k_x and k_z are the wavenumbers along the x- and z- directions, respectively. The correlation length is $a = \sqrt{a_x^2 + a_z^2}$. A wide range of values have been associated with the von-Karman parameters for the earth subsurface. The values of the von-Karman parameters depend on the subsurface lithology and the depth of the subsurface. Using the autocorrelation function of surface rock samples from Westerly and Oshima granite, *Spetzler et al.* (2002) estimate for the Westerly granite $\epsilon = 8.5$ % and $a = 0.22\ mm$ while $\epsilon = 9.3$ % and $a = 0.46\ mm$ for the Oshima granite. *Yoshimoto and Sato* (1997), using 149 waveforms in the frequency band of 8 - 16 Hz from 10 earthquakes occurring at depths shallower than 10 km, estimates the range of ϵ and a values to be 5 - 8 % and 0.3 - 0.8 km, respectively, in the Nilko area of Japan.

The scattering model we use for kernel computation consists of the random velocity fluctuations defined by the von-Karman parameters and constant density. The velocity model is given as

$$v(\mathbf{x}) = v_0(\mathbf{x})[1 + \zeta(\mathbf{x})], \quad (7)$$

where $v_0(\mathbf{x})$ is the background velocity and $\zeta(\mathbf{x})$ is a realization of the random velocity fluctuation for the von-Karman PSDF in equation 6 (*Sato et al.*, 2012).

3.1 Numerical vs. analytical computation

The sensitivity kernel can be estimated from analytical models of the scattered intensity (the diffusion and radiative transfer approximation of the scattered intensity). To compare the analytical and numerical solution of the sensitivity kernel, we use a von-Karman scattering model defined by the following parameters: $a_x = a_y = 0.01\ km$, $\epsilon = 0.1$, $\kappa = 0.5$, and $f = 15\ Hz$ ($\lambda = 0.23\ km$). This scattering model and the dominant scattering wavenumber correspond to $ka \simeq 0.27$. The scattering velocity model is given in Figure 1 with an average velocity of 3.5 km/s. The theoretical scattering mean free path (l_{VK}) and transport mean free path (l^*_{VK}) for these von-Karman parameters and the scattered waves are 5.7 km and 6.9 km, respectively (*Sato et al.*, 2012).

We compute the analytical solution of the sensitivity kernel by using the corresponding theoretical mean free path lengths and the approximations of the scattered intensity using the diffusion (equation 4) and the radiative transfer (equation 5) models. We also convolve the analytical intensities with the intensity of the source wavelet used for the computation of the numerical kernel. Figures 2, 3 and 4 show time snapshots of the temporal evolution of the sensitivity kernel for both the numerical and the analytical solutions, respectively. In Figures 2, 3 and 4, the time-shots are taken at 0.95 s, 1.20 s, 2.00 s, and 4.00 s. The numerical solution of the sensitivity kernel is bound by the a kernel front which is defined as the edge of the kernel that is dominantly composed of single scattering and bounds the

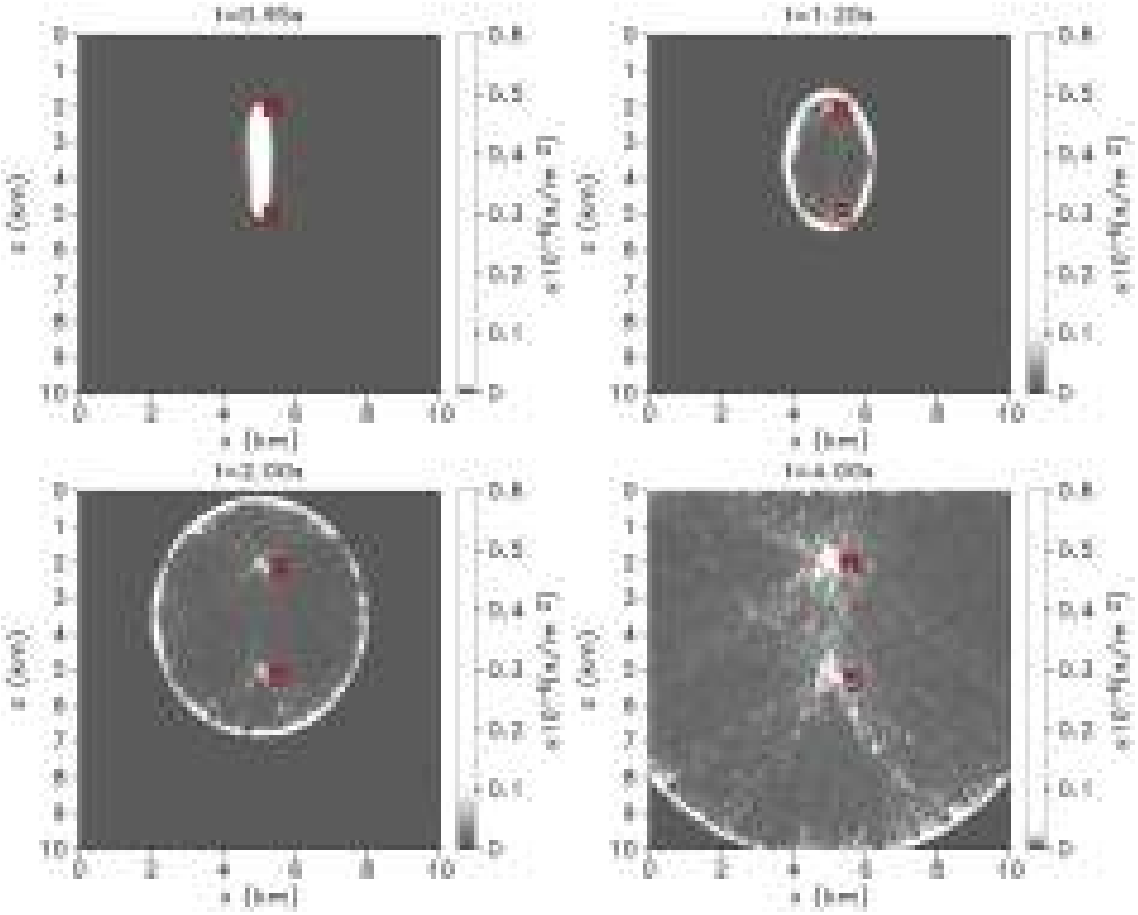

Figure 2. Temporal and spatial evolution of the sensitivity kernel (numerical solution).

multiple scattering contributions. The numerical sensitivity kernel shows similar features represented in the radiative transfer model (Figures 3) of the sensitivity kernel including the direct line-of-sight characteristic of the ballistic kernel (0.95 s) and the elliptical shape of the kernel front at lapse times after the first arrival time. The major difference between the numerical kernel and the radiative transfer kernel is the fluctuations in the numerical kernel. The numerical kernel in Figure 2 is computed with one realization of the scattering model. These kernel fluctuations are suppressed by averaging the numerical kernel over many realizations of the scattering model. The diffusion approximation of the sensitivity kernel (Figures 4), as expected, only reproduces the spatial features of the kernel at long lapse times ($ct/R_{sr} \gg 1$) (*Paasschens*, 1997) with no clear ellipsoidal edge. Figure 5 shows a cross-section of the kernel along the source-receiver line. The diffusion kernel fails to explain the zero or near-zero sensitivity of the kernel beyond the kernel front, evident in both the numerical and the radiative transfer kernels.

The spatial and temporal behavior of the kernel implies that to resolve time-lapse changes within a scattering medium with homogeneous statistical properties, the radiative transfer kernel can closely substitute for the numerical kernel solution. Figure 5 shows that the numerical kernel has more fluctuations compared to the analytical solutions. This numerical kernel is computed with one realization of the scattering model. The kernel fluctuations which are due to isolated scatterers within the scattering model, are present in the multiply scattering contribution to the kernel. We can suppress the kernel fluctuations by averaging the kernel over a number of the realizations of the scattering model with the same statistical properties. Figure 6 shows the averaged kernel at travel-time 2.00 s over 1, 5, 10 and 20 realizations of the scattering model. Increasing the number of realizations of the model used for the kernel computation reduces the fluctuations both at the singly scattered and multiply scattered part of the kernel. With few realizations of the random model (5-10 realizations) we can achieve stability in the sensitivity kernel (Figure 7).

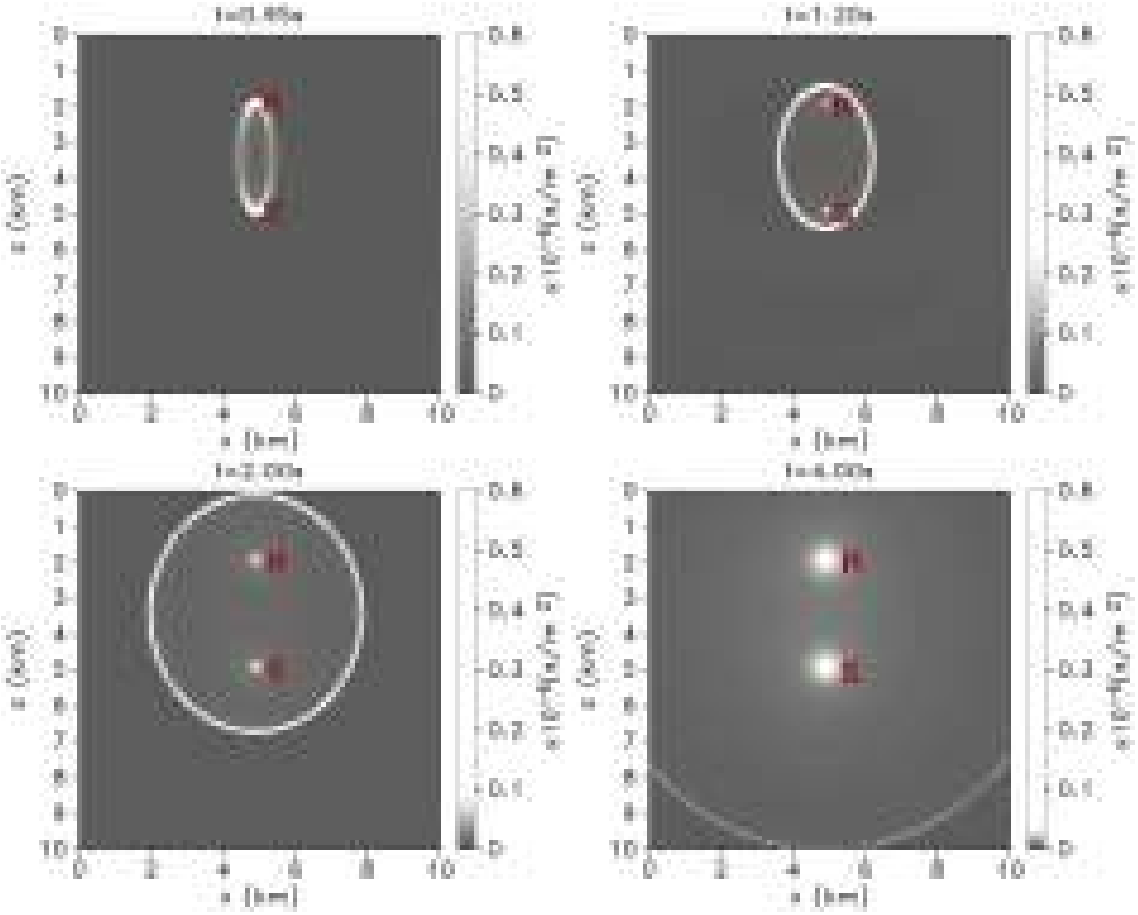

Figure 3. Temporal and spatial evolution of the sensitivity kernel using the radiative transfer model.

3.2 Scattering Velocity models

3.2.1 Random isotropic scattering model

Figure 2 shows the kernel for a given source-receiver pair (S-R) at the following time snapshots: 0.95 s, 1.20 s, 2.00 s, and 4.00 s. The direct wave excited by a source S arrives at the receiver R at travel-time $t = 0.90$ s with an average velocity of 3.5 km/s. The time snapshots of the kernel shown in Figure 2 show the sensitivity to the changes in the scattering model for the scattered phases arriving at a specific travel-time t. The kernel at $t = 0.95$ s corresponds to the sensitivity of scattered waves dominated by direct and forward scattered waves. With increasing time, the area covered by the sensitivity kernel progressively increases. The spatial broadening of the kernel with time increases the detectability of any change in the scattering property of the medium due to multiple interaction between the scattered waves and the change with time, especially changes away from the path of the direct wave (which is along the source-receiver line in this case). However, the resolving power of the kernel is expected to decrease with increasing time because of the spatial broadening of the kernel. The shape of the kernel with increasing time depends on the source and receiver locations, the corresponding travel-time, and the properties of the scattering medium. At times $t > 0.95$ s, the kernel assumes an elliptical shape with the major axes along the source-receiver line and the minor axes perpendicular to the source-receiver line. The edge of the kernel is dominated by contributions from single scattering. The kernel for the singly scattered waves is given by (*Pacheco and Snieder*, 2006)

$$K(\mathbf{x_o}, t) = \frac{1}{2\pi h\sqrt{(ct/R_{sr} - 1)}}\left[\frac{r_s}{s} + \frac{r_r}{r}\right], \quad (8)$$

where s and r are the distances from the point $\mathbf{x_o}$ to the source and receiver, respectively; r_s and r_r are the distances from any point on the kernel front to the source and receiver, respectively.

The single-scattering-dominated part of the kernel spatially bounds the multiple scattering part of the kernel. The inner part of the kernel accounts for multiple scattering, which has lower amplitude compared to the kernel contribution from the single scattering. Within the multiple-scattering-dominated part of the kernel,

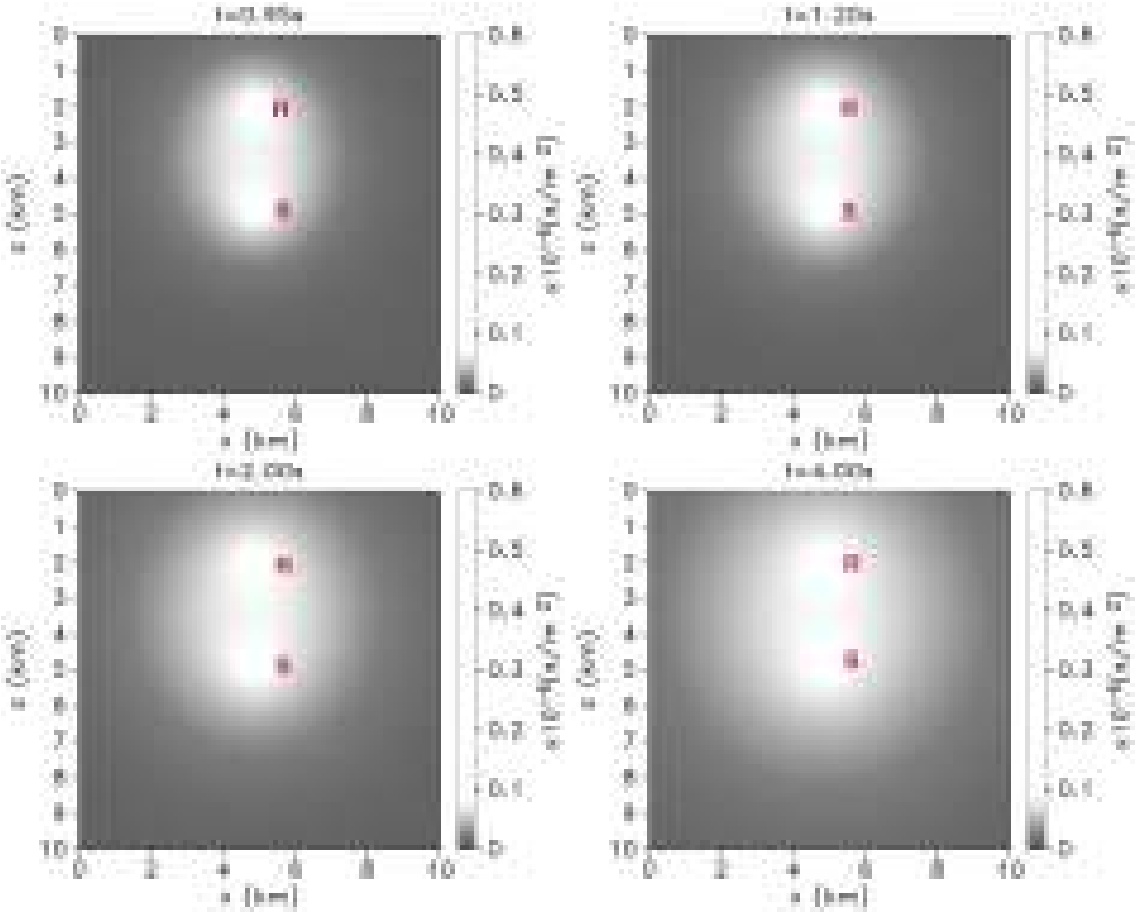

Figure 4. Temporal and spatial evolution of the sensitivity kernel using the diffusion model.

there are high sensitivities at the source and receiver locations which are predicted accurately by the analytical solutions in Figures 5. These high sensitivities at or near the source and receiver locations suggest that the dominant contribution to the multiply scattered waves recorded at receiver R due to a source S originates from scattering near the source and receiver locations.

3.2.2 Random non-isotropic scattering model

The scattering properties within the earth's subsurface are generally complex and inhomogeneous. The scattering characteristics of the subsurface can vary from place to place depending on both the underlying lithology and overlaying stress conditions of the local and regional subsurface. The scattering properties of the earth's subsurface also vary with depth (*Shearer and Earle*, 2008). The stress- and depth- dependent scattering properties of the subsurface controls the scattering process of the seismic wave traveling through the subsurface. The effective scattering of the subsurface are defined by both the scattering properties of the subsurface and the characteristics of the incident seismic phase that is scattered. The characteristics of the incident phase include the incidence angle of the wave, the spectral properties of the incident wave, and the wave mode of the incident wave (*Levander*, 1990).

To explore the dependence of the sensitivity kernel on the scattering medium, we test two scattering models whose background velocity is a 3-layered velocity model. In both models (Figures 8 and 11), the top and bottom layers have the same scattering properties given by the von-Karman PSDF. For the top layer, $\kappa = 0.5$, $\epsilon = 0.5$, and $a_z = a_x = 0.05\ km$; for the bottom layer, $\kappa = 0.8$, $\epsilon = 0.1$, and $a_z = a_x = 0.1\ km$. However, in the middle layer, one model consists of vertical velocity perturbations while the other model is composed of horizontal velocity perturbations. The model with vertical velocity perturbations mimics a highly vertically fractured reservoir while the model with horizontal velocity perturbations represents a shale-like reservoir with a thin laminated layering. The middle layer for both models is defined by the following von-Karman parameters. For the vertically fractured model, $a_z = 0.5\ km$

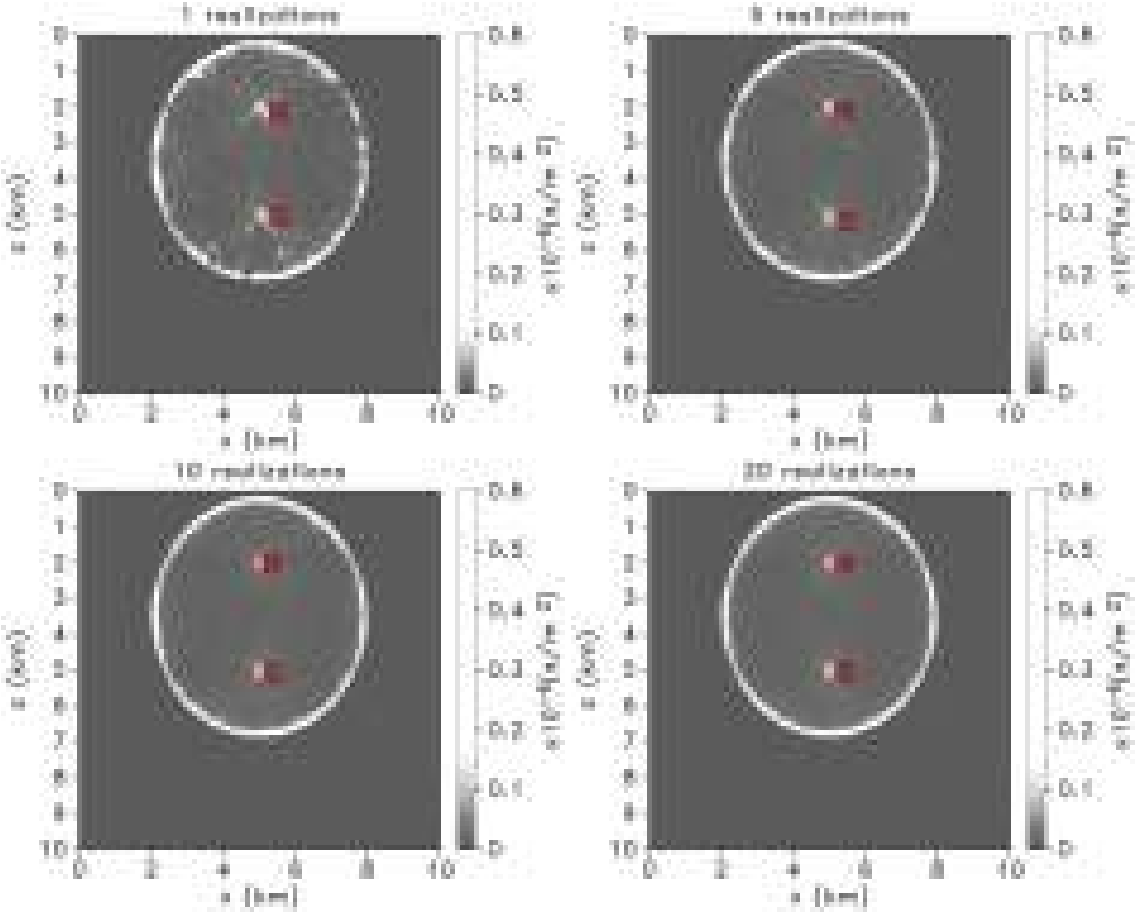

Figure 6. Compassion of the kernel at $t = 2.0\ s$ using a number of scattering model realizations

and $a_x = 0.0001\ km$; for the shale-like model, $a_z = 0.0001\ km$ and $a_x = 0.5\ km$. In both models, $\kappa = 0.1$ and $\epsilon = 0.5$ for the middle layer. In both scattering models, we compute the sensitivity kernels using two source-receiver configurations. In one configuration, the source-receiver line is vertical while in the second configuration the source-receiver line is horizontal and is embedded within the middle layer. These source-receiver configurations resemble a source such as a microseismic event or an earthquake embedded within the subsurface with either a receiver at the near surface (for the vertical source-receiver line) or a receiver within a borehole (for the horizontal source-receiver line).

Figures 9 and 10 give time snapshots of the sensitivity kernel in the vertically fractured model for the vertical and horizontal source-receiver configurations, respectively. In both source-receiver configurations, the kernels show many of the features present in the kernel of the random isotropic model (Figure 2), which include the spatial broadening of the kernel with increasing time, the high sensitivity at the source and receiver locations, and the presence of the single scattering contributions to the kernel at the kernel front. However, the heterogeneity in the scattering model introduces extra features to the kernel of the vertically fractured model which are not present in the random isotropic kernel (Figure 2). In both source-receiver configurations, the width of the kernel (along the minor axes of the kernel) at each layer of the model depends on the effective velocity in that layer (see Figures 9 and 10 at $t = 2.50\ s$). In the vertical source-receiver configuration at $t = 2.50\ s$ and $5.00\ s$, there are extra scattered fronts marked as $S^{''}$ within the kernel; these fronts are secondary scattered intensity fronts due to reflections from the layer interfaces in the model. These reflected fronts lag behind the singly scattered front. In the horizontal source-receiver configuration (Figure 10), the direct wave refracts through the top interface of the bottom layer because of the higher velocity of the bottom layer (Figure 10 at $t = 1.38\ s$). A few milliseconds later, many of the forward scattered waves are confined within the middle layer (Figure 10 at $t = 1.40\ s$). At later lapse times, the singly scattered kernel front propagates out from the middle layer into the top and the bottom lay-

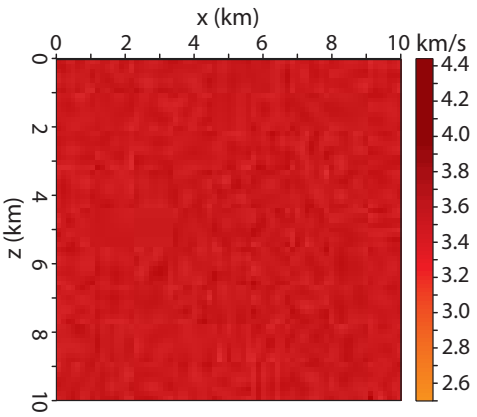

Figure 1. Velocity model for numerical computation of sensitivity kernel for comparison with the analytical solution.

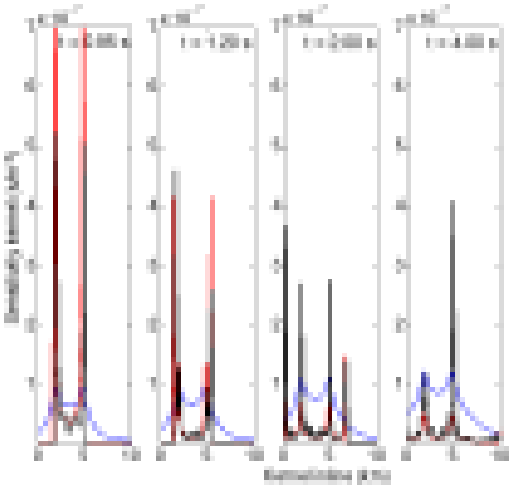

Figure 5. Comparison between numerical sensitivity kernel (black line) and diffusion- (blue line) and radiative transfer- (red line) based kernel along the source- (at 2 km) receiver- (at 5 km) line.

ers. The extent of the front propagation depends on the average velocity of the layer. The reflected wavefronts S'' seen in the vertical source-receiver configuration are absent in the kernel with the horizontal source-receiver configuration. This is because the reflectors are parallel to the source-receiver line in the horizontal configuration. The sensitivity is dominant within the middle layer because the vertical velocity perturbations within the middle layer persistently reflects back and forth waves traveling horizontally between the source and the receiver. The orientations of the velocity perturbations are perpendicular to the dominant forward propagation of the waves which is along the source-receiver line (Fig-

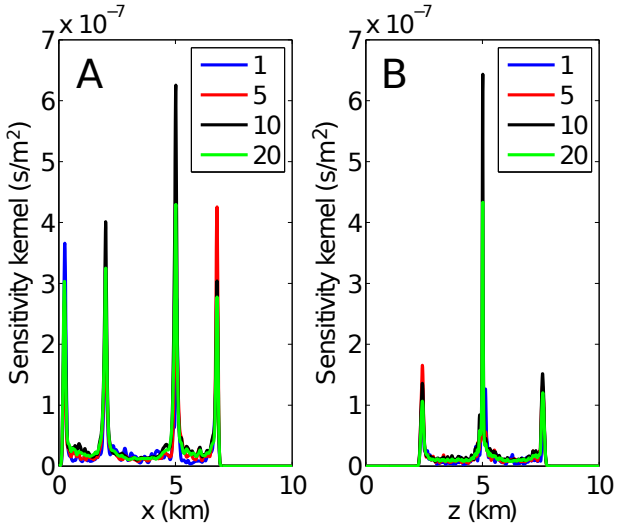

Figure 7. The inline section (A) and the crossline section (B) of the kernel at $t = 2.0$ s after averaging over 1, 5, 10, and 20 realizations of the scattering model with the same statistical properties.

ure 10 at $t = 2.50$ s and 5.00 s). This dominance of the kernel in the middle layer is not present with the vertical source-receiver setup (Figure 9), where in the middle layer the wave propagation direction is along the direction of the velocity perturbation. The lack of the kernel dominance within the middle layer with a vertical source-receiver setup is because of the relative orientation of the source-receiver line and the orientation of the scatterers which results to minimal scattering of the waves compared to the horizontal source-receiver setup. Also the scattered waves recorded at the receiver has a higher probability of exploring the whole model space without being trapped within middle layer due to scattering. With the horizontal source-receiver setup, much of the recorded scattered waves are generated within the middle layer.

Figures 12 and 13 give time snapshots of the sensitivity kernel in the shale-like model using the vertical and horizontal source-receiver configurations, respectively. The kernel for the shale-like model, which uses a vertical source-receiver configuration, exhibits similar features present in the vertically fractured model with a similar source-receiver setup. Differences in the kernels are in the multiply scattered part of the kernel in the middle layer of the vertically fractured model where there are more scattering close to the source. However, with the horizontal source-receiver configuration (Figure 13), the kernel at late lapse time ($t = 2.50$ s and 5.00 s) shows features different from those present in the kernel with the vertically fractured model using the horizontal source-receiver configuration. The high sensitivity present in the vertically fractured model using the horizontal source-receiver setup is absent from the

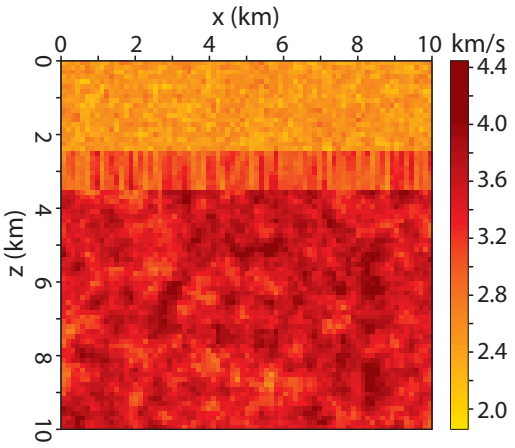

Figure 8. Velocity model with a vertical-fractured-like reservoir.

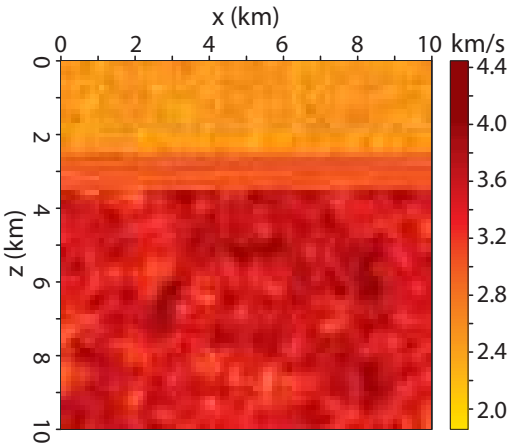

Figure 11. Velocity model with a shale-like reservoir.

model with the horizontal velocity perturbation in the middle layer because the direction of wave propagation between the source and the receiver is parallel to the velocity layering in the middle layer, which results in relatively less scattering of the seismic wave. The effect of the source-receiver setup on the kernel behavior implies that the setup of the source and receiver pairs relative to the location of a particular time-lapse change within a scattering medium has large implications for the capability of detecting and resolving the time-lapse change. For example, if there is a change in the middle layer, the horizontal source-receiver setup provides a better scenario for detecting and resolving the time-lapse change in the middle layer than will the vertical source-receiver setup. This connection between the source-receiver setup and the behavior of the sensitivity kernel suggests the need for the source and receiver to be in close proximity to the location of the time-lapse change. The relative direction of the forward scattering between the source and the receiver to the orientation of the length of the scatterers impacts the relative magnitude of the sensitivity of the scattered intensity to the time-lapse change. This impact is evident in a comparison of the kernel strength in the middle layers of the vertically fractured model to the kernel strength in the middle layer of the shale-like model. The relative strength of the kernel is higher in the vertically fractured model where the perpendicular alignment of the scatterers allows for a stronger generation of multiply scattered waves.

The kernels at early lapse times are almost identical in both models (Figures 9, 10, 12 and 13 at $t = 1.38\ s$ and $1.40\ s$). The kernels at these times consist of mainly direct, refracted, and forward scattered waves.

3.3 Topography-induced Scattering

Seismic waves are not only scattered by heterogeneities within the earth's subsurface, but also by near-surface heterogeneities such as variable topography or low velocity unconsolidated lithology in the near-surface layers. Due to the high impedance contrast across the free surface and the higher heterogeneities within the near-surface compared to the heterogeneities deeper in the subsurface (*Shearer and Earle*, 2008), the multiple scattering from variable topography and near-surface scattering effects can dominate bulk scattering. Rough or variable topography plus the presence of the free surface can focus or defocus seismic waves and can convert seismic waves from one wave mode to another such as conversion of body waves to surface waves and vice versa (*Levander*, 1990). *Bouchon et al.* (1996) show that a simple symmetric ridge can induce amplification of a monochromatic SH wave by up to a factor of 1.5 at the crest of the ridge. The amplification factor of the incident wave depends on the incident angle of the wave and the height to width ratio of the topography perturbation.

To explore the effect of topography on the sensitivity kernel, we simulate an acoustic wavefield using a homogeneous velocity model with a variable topography. The velocity model consists of 3 homogenous layers: a top air layer with a velocity of 330m/s, a thin layer under the topography with a velocity of 2000 m/s, and the rest of the model with a velocity of 3000 m/s (Figure 14). The free-surface is approximated using the air-subsurface interface based on the velocity discontinuity assuming a constant density (*Taillandier et al.*, 2009). We model the variable topography using a 1D von-Karman PSDF in order to create a random vari-

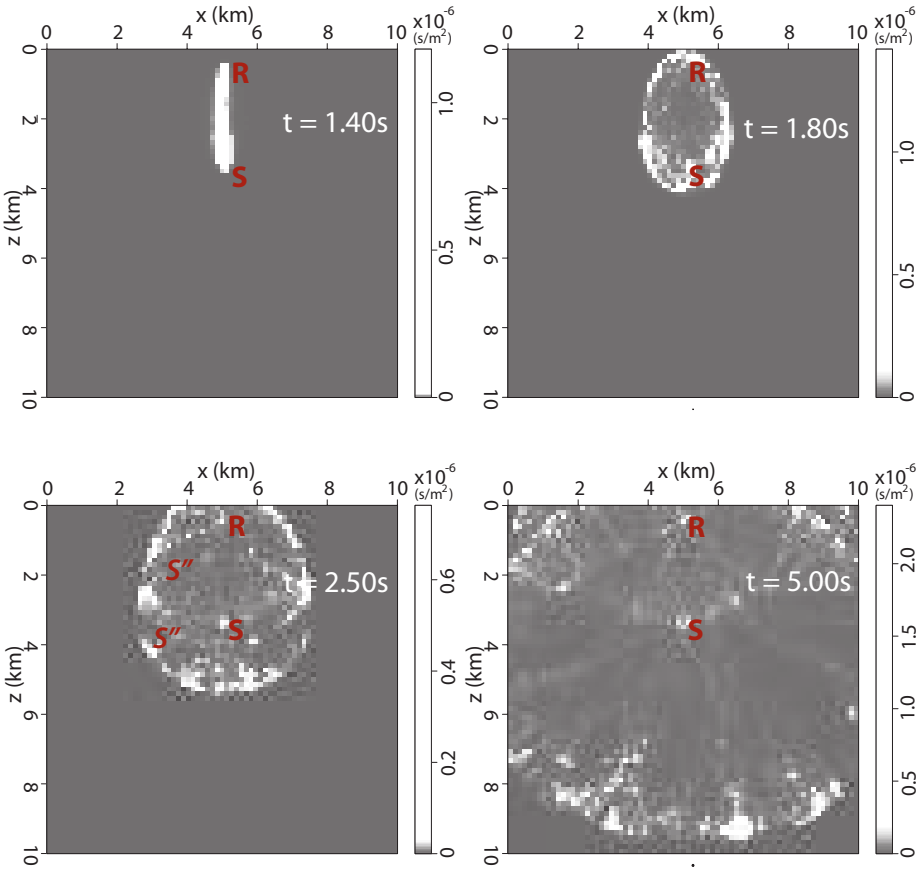

Figure 9. Temporal and spatial evolution of the sensitivity kernel (numerical solution) in a reservoir with vertical-fractured-like velocity perturbation with a near-surface receiver. S'' corresponds to the reflected scattered phase.

able topography with a correlation across the topography defined by a correlation distance of 0.5 *km*.

We compute the sensitivity kernel with the scattered waves induced by the variable topography using a vertical source-receiver setup (Figure 15) and a horizontal source-receiver setup (Figure 16). At time $t = 1.40$ *s*, the kernel accounts for the direct wave between source S and receiver R. The direct wave kernel using the vertical source-receiver setup is shown in Figure 15 at $t = 1.40$s. At later lapse time (Figure 15; $t > 1.40$ *s*), the kernel expands into a singly scattered front which broadens with time. The kernel has a relatively large magnitude within the tiny low velocity layer underneath the topography (Figure 15, $t = 2.5$ *s* and 5.0 *s*). This part of the kernel is due to scattering contributions from the topography-induced scattering which are trapped in the near-surface layer. This topography-induced sensitivity is contained predominantly within the near-surface layer by the velocity interface on top of the high velocity halfspace. The topography-induced sensitivity, however, increases and broadens away from the receiver location within the near-surface layer with an increase in time.

When the source and receiver are embedded within the near-surface layer underneath the variable topography, the kernel of the first arrival consists of refracted waves off of the higher velocity halfspace underneath the near-surface low velocity layer (Figure 16, $t = 1.6$ *s*). Similar to the vertical source and receiver setup, the direct/refracted kernel with the horizontal source and receiver setup splits for t= 1.8 *s* into the singly scattered kernel. In Figure 16, only the downward section of the singly scattered kernel is present because the high velocity contrast across the topography prevents propagation of scattered waves into the air. At later lapse time ($t = 2.50$ *s* and 5.00 *s*, Figure 16), the dominant part of the kernel lies within the low velocity layer which results from the topography-induced scattering and the trapped waves within the low velocity layer. The presence of the thin low velocity layer underneath the topography induces kernels with similar behavior at large lapse time for both source-receiver setups.

The behavior of the kernel in the presence of variable topography and a thin low velocity layer in the above results demonstrates the need to accurately char-

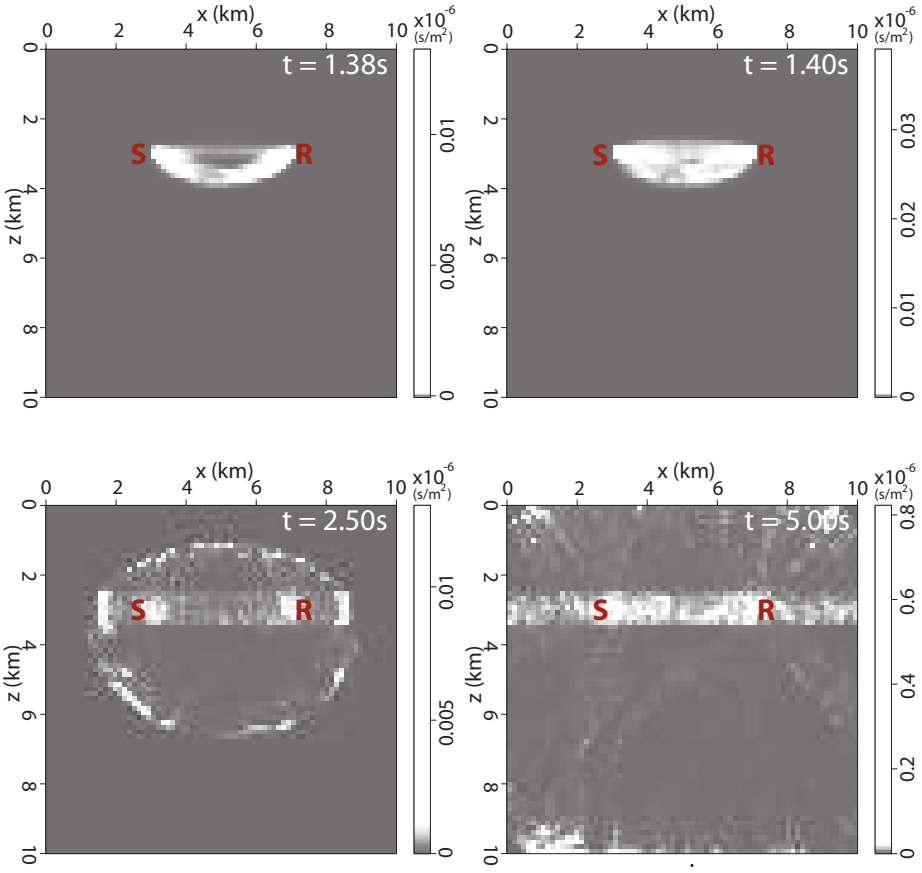

Figure 10. Temporal and spatial evolution of the sensitivity kernel (numerical solution) in a reservoir with vertical-fractured-like velocity perturbation with a receiver within the reservoir.

acterize the scattering properties of the medium being monitored. Incorporating both the topography and the appropriate velocity (scattering) model in the kernel computation provides the distribution and origin of the scattered waves via the kernel that can be used for time-lapse monitoring. Due to the effect of variable topography and of a heterogeneous scattering medium on the kernel, we will need to use an appropriate source-receiver array setup to image a time-lapse change within the subsurface. For example, in a case of monitoring velocity changes within a reservoir that might be due to fluid production or injection within the reservoir, a borehole array in close proximity to the change might be a more effective source-receiver setup for monitoring than using a surface-receiver array. In this case, the borehole array records more of the scattered waves generated within a given layer. This results in higher sensitivity to a change in that layer. Also, the borehole array, depending on its relative depth to the free-surface, will have less of the topography- or near-surface- induced scattering.

4 DISCUSSION AND CONCLUSION

We propose a novel approach to compute the sensitivity kernel that can be used to resolve weak changes within the earth's subsurface or any other medium using multiply scattered waves. These are changes which are usually irresolvable with singly scattered waves. Our approach does not rely on analytical models of the scattered intensity such as the diffusion and radiative transfer models. To compute the sensitivity kernel, we compute the scattered intensity field needed for the kernel computation using an a prior model of the scattering medium from numerically generated scattered wavefield. In this paper, we use the finite-difference modeling for the computation of the seismic wavefield. The numerical modeling of the scattered intensity can take advantage of various numerical methods for seismic wavefield computation. Using our approach we can incorporate any complexities of the scattering medium and any boundary conditions of the medium. With an appropriate a prior scattering model, we can obtain a more accurate estimate of the sensitivity kernel which accurately describes

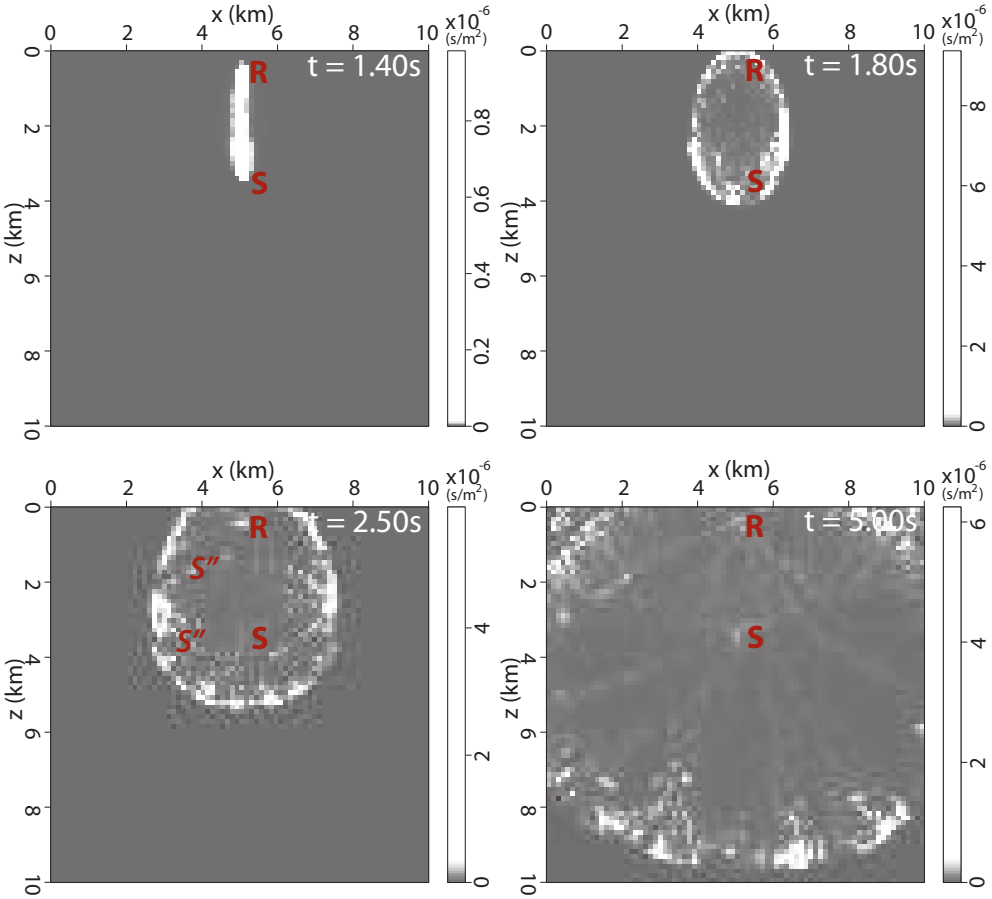

Figure 12. Temporal and spatial evolution of the sensitivity kernel (numerical solution) in a reservoir with shale-like velocity perturbation. S'' corresponds to the reflected scattered phase.

the intensity of the scattered wave recorded by a given source-receiver pair. Our kernel computation approach is suitable for a medium such as the earth's subsurface where in most cases the scattering properties are heterogeneous and whose scattered intensity may not be described analytically.

The caveat to the computation of the scattered intensity and in extension the sensitivity kernel for the time lapse monitoring, are the computation cost of both the scattered intensity and the corresponding kernel and the need for an accurate a prior model of the statistical properties of the scattering medium. The cost of the kernel computation mostly depends on the traveltime of the scattered phase for the kernel, the sum of number of sources and receivers, the number of the scattering model realizations needed, the cost of the forward modeling of the scattered intensity for both the source and receiver intensity fields, and the cost for the convolution between the source and receiver intensity fields. The cost for the forward modeling of the scattered intensity depends on the spatial dimensions of the scattering model used for modeling the intensity field which makes a significant difference if the medium is 2D or 3D and the temporal or the frequency dimension of the scattered waves. All numerical examples we show in this paper uses 2D models but the computation of the numerical kernel in 3D follows exactly the same procedure.

Another limitation of the numerical computation of the sensitivity kernel is the need to know the statistical property of the a prior model. This limitation is also inherent to the analytical computation of the kernel where the scattering parameter such the diffusion coefficient and the mean free path length are needed for the diffusion and the radiative transfer models, respectively. The details of the a prior scattering model needed for the kernel computation can be relaxed, with the requirement that the a prior model used should have similar statistical property to that of the true model and that the corresponding scattered intensity should explain significantly the envelope of the scattered wave rather than the individual phases of the multiply scattered waves. The effect of the fluctuations in the microscopic properties between the a prior scattering model and the true scattering medium can be suppressed while computing

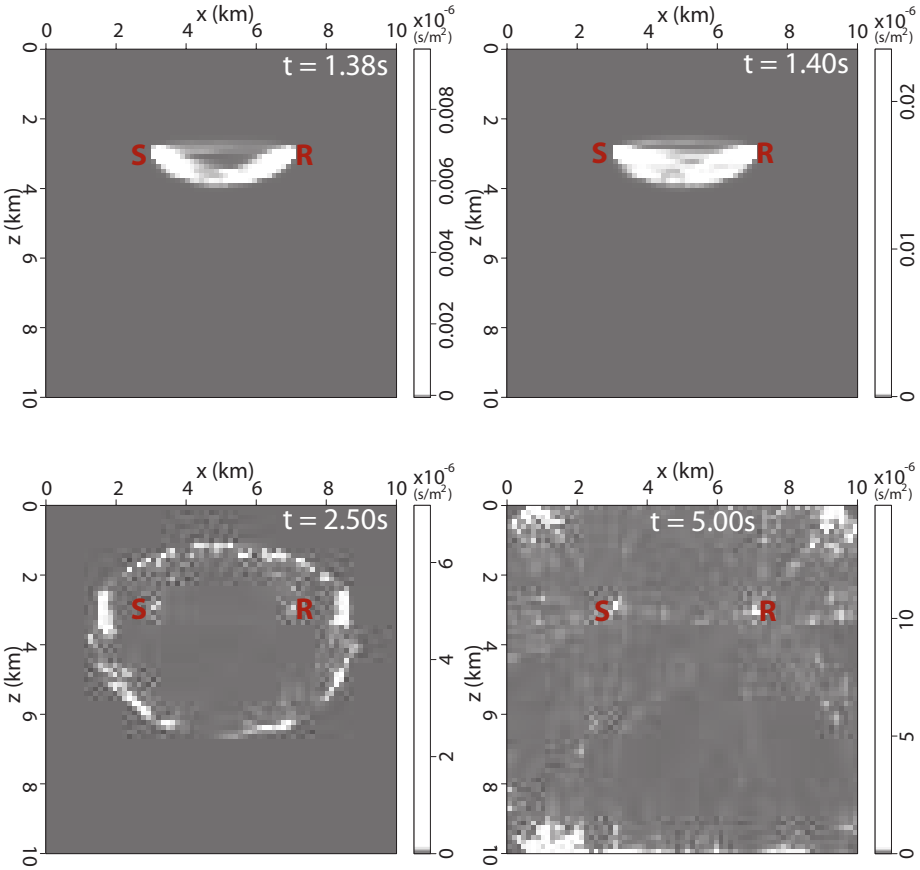

Figure 13. Temporal and spatial evolution of the sensitivity kernel (numerical solution) in a reservoir with shale-like velocity perturbation.

the kernel with multiple realizations of the scattering model. A few realizations of the scattering model (for example, 5-10 realizations) can significantly stabilize the fluctuations in the sensitivity kernel.

The numerical examples in this study are based on acoustic wave propagation with isotropic source radiation. This acoustic wave assumption can be considered valid at the equipartition regime of multiply scattered waves at which S-wave energy dominates the scattered waves (*Weaver*, 1982; *Hennino et al.*, 2001). Equipartitioning of the scattered waves is achieved late in the coda (traveltimes at which diffusion approximation is usually considered). However, our recipe for computing the numerical sensitivity kernel remains valid for elastic wave propagation. For elastic waves, we expect to get the sensitivities to the change in P- and S-wave velocities. The computation of the elastic sensitivity kernels will involve additional considerations. Some of these considerations include, separating the P- and S- wave modes in order to get the sensitivities to P- and S-wave velocity changes and using the appropriate radiation pattern for the receiver intensity field that depends on

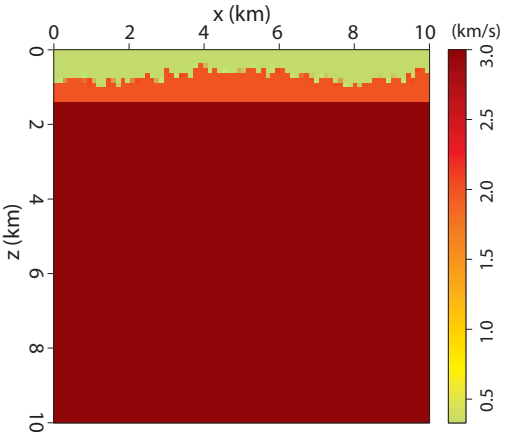

Figure 14. Velocity model with variable topography.

the propagation directions of either the recorded P-wave or S-wave. The details on the elastic sensitivity kernel will be in a forthcoming publication.

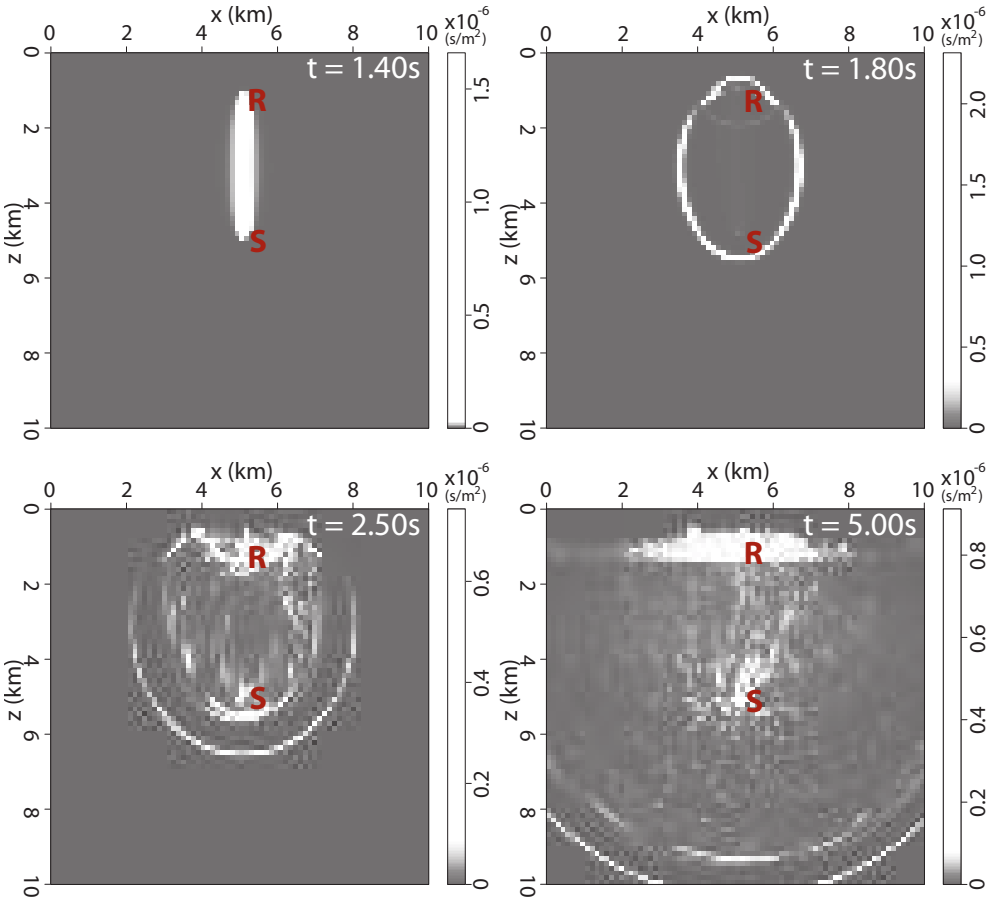

Figure 15. Temporal and spatial evolution of the sensitivity kernel (numerical solution) showing topography-induced scattering using vertical source-receiver line.

ACKNOWLEDGMENTS

This research was supported by sponsors of the Consortium Project on Seismic Inverse Methods for Complex Structures. The reproducible numerical examples in this paper use the Madagascar open-source software package freely available from http://www.ahay.org.

REFERENCES

Belkebir, K., P. C. Chaumet, and A. Sentenac, Influence of multiple scattering on three-dimensional imaging with optical diffraction tomography, *Journal of the Optical Society of America A*, *23*, 586–595, 2006.

Berkhout, A., D. Verschuur, and G. Blacquire, Illumination properties and imaging promises of blended, multiple-scattering seismic data: a tutorial, *Geophysical Prospecting*, *60*, 713–732, 2012.

Bouchon, M., C. A. Schultz, and M. N. Toksz, Effect of three-dimensional topography on seismic motion, *Journal of Geophysical Research: Solid Earth*, *101*, 5835–5846, 1996.

Fleury, C., Increasing illumination and sensitivity of reverse-time migration with internal multiples, *Geophysical Prospecting*, *61*, 891–906, 2013.

Gaburro, R., C. J. Nolan, T. Dowling, and M. Cheney, Imaging from multiply scattered waves, vol. 6513, pp. 304–311, 2007.

Haney, M. M., K. van Wijk, and R. Snieder, Radiative transfer in layered media and its connection to the O'Doherty-Anstey formula, *Geophysics*, *70*, T1–T11, 2005.

Hennino, R., N. Trégourès, N. Shapiro, L. Margerin, M. Campillo, B. Van Tiggelen, and R. Weaver, Observation of equipartition of seismic waves, *Physical Review Letters*, *86*, 3447–3450, 2001.

Levander, R., A., Seismic scattering near the earth's surface, *Pure and Applied Geophysics*, *132*, 21–47, 1990.

Malcolm, A. E., B. Ursin, and M. V. De Hoop, Seismic imaging and illumination with internal multiples, *Geophysical Journal International*, *176*, 847–

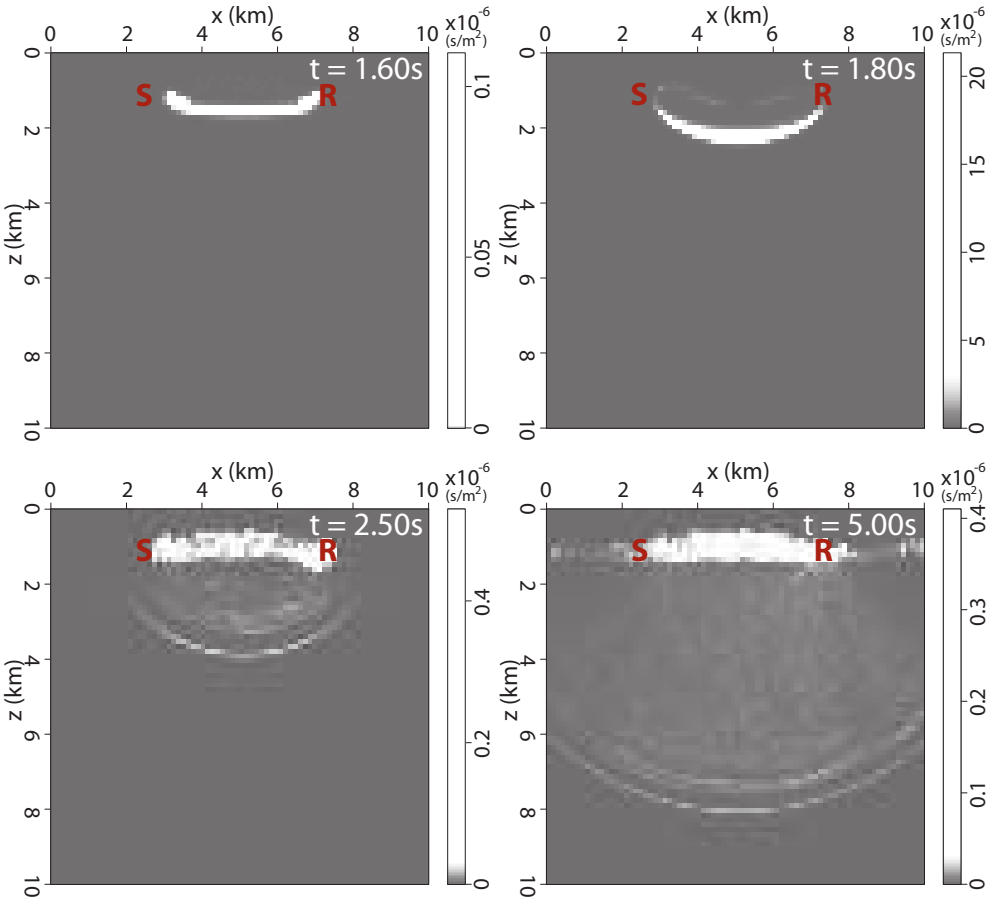

Figure 16. Temporal and spatial evolution of the sensitivity kernel (numerical solution) showing topography-induced scattering using horizontal source-receiver line.

864, 2009.

Margerin, L., and H. Sato, Reconstruction of multiply-scattered arrivals from the cross-correlation of waves excited by random noise sources in a heterogeneous dissipative medium, *Wave Motion*, *48*, 146–160, 2011.

Margerin, L., M. Campillo, and B. van Tiggelen, Radiative transfer and diffusion of waves in a layered medium: new insight into coda q, *Geophysical Journal International*, *134*, 596–612, 1998.

Masera, D., P. Bocca, and A. Grazzini, Frequency analysis of acoustic emission signal to monitor damage evolution in masonry structures, *Journal of Physics: Conference Series*, *305*, 012,134, 2011.

Nishimura, T., N. Uchida, H. Sato, M. Ohtake, S. Tanaka, and H. Hamaguchi, Temporal changes of the crustal structure associated with the M6.1 earthquake on September 3, 1998, and the volcanic activity of Mount Iwate, Japan, *Geophysical Research Letters*, *27*, 269–272, 2000.

Paasschens, J. C. J., Solution of the time-dependent Boltzmann equation, *Physical Review E*, *56*, 1135–1141, 1997.

Pacheco, C., and R. Snieder, Time-lapse travel time change of multiply scattered acoustic waves, *The Journal of the Acoustical Society of America*, *118*, 1300–1310, 2005.

Pacheco, C., and R. Snieder, Time-lapse traveltime change of singly scattered acoustic waves, *Geophysical Journal International*, *165*, 485–500, 2006.

Page, J. H., H. P. Schriemer, A. E. Bailey, and D. A. Weitz, Experimental test of the diffusion approximation for multiply scattered sound, *Physical Review E*, *52*, 3106–3114, 1995.

Poupinet, G., W. L. Ellsworth, and J. Frechet, Monitoring velocity variations in the crust using earthquake doublets: An application to the Calaveras fault, California, *Journal of Geophysical Research*, *89*, 5719–5731, 1984.

Ripoll, J., M. Nieto-Vesperinas, and S. R. Arridge, Effect of roughness in nondiffusive regions within diffusive media, *Optical Society of America OCIS*, *18*, 940–947, 2001.

Rossetto, V., Local time in diffusive media and ap-

plications to imaging, *Physical Review E*, *88*, 2013, arXiv:1307.4867.

Rossetto, V., L. Margerin, T. Planès, and E. Larose, Locating a weak change using diffuse waves: Theoretical approach and inversion procedure, *Journal of Applied Physics*, *109*, 034,903, 2011.

Sato, H., M. C. Fehler, and T. Maeda, *Seismic Wave Propagation and Scattering in the Heterogeneous Earth : Second Edition: Second Edition*, Springer, 2012.

Schaff, D. P., and G. C. Beroza, Coseismic and postseismic velocity changes measured by repeating earthquakes, *Journal of Geophysical Research*, *109*, 2004.

Shapiro, S. A., and G. Kneib, Seismic attenuation by scattering: Theory and numerical results, *Geophysical Journal International*, *114*, 373–391, 1993.

Shearer, M., P., and S. Earle, P., Observing and modeling elastic scattering in the deep earth, *Advances in Geophysics*, *50*, 167–194, 2008.

Snieder, R., A. Grt, H. Douma, and J. Scales, Coda wave interferometry for estimating nonlinear behavior in seismic velocity, *Science*, *295*, 2253 –2255, 2002.

Spetzler, J., C. Sivaji, O. Nishizawa, and Y. Fukushima, A test of ray theory and scattering theory based on a laboratory experiment using ultrasonic waves and numerical simulation by finite-difference method, *Geophysical Journal International*, *148*, 165–178, 2002.

Taillandier, C., M. Noble, H. Chauris, and H. Calandra, First-arrival traveltime tomography based on the adjoint-state method, *Geophysics*, *74*, WCB1–WCB10, 2009.

Turner, J. A., and R. L. Weaver, Radiative transfer and multiple scattering of diffuse ultrasound in polycrystalline media, *The Journal of the Acoustical Society of America*, *96*, 3675–3683, 1994.

Vlastos, S., E. Liu, I. G. Main, M. Schoenberg, C. Narteau, X. Y. Li, and B. Maillot, Dual simulations of fluid flow and seismic wave propagation in a fractured network: Effects of pore pressure on seismic signature, *Geophysical Journal International*, *166*, 825–838, 2006.

Weaver, R., On diffuse waves in solid media, *J. Acoust. Soc. Am.*, *71*, 1608–1609, 1982.

Wegler, U., and C. Sens-Schnfelder, Fault zone monitoring with passive image interferometry, *Geophysical Journal International*, *168*, 1029–1033, 2007.

Wesley, J. P., Diffusion of seismic energy in the near range, *Journal of Geophysical Research*, *70*, 5099–5106, 1965.

Yodh, A., and B. Chance, Spectroscopy and imaging with diffusing light, *Physics Today*, *48*, 34, 1995.

Yoshimoto, K., and H. Sato, Short-wavelength crustal heterogeneities in the Nikko area, Central Japan, revealed from the three-component seismogram envelope analysis, *Physics of The Earth and Planetary Interiors*, *104*, 63–73, 1997.